#### **OPEN ACCESS**



# **Bound Debris Expulsion from Neutron Star Merger Remnants**

Yossef Zenati<sup>1,8</sup>, Julian H. Krolik<sup>1</sup>, Leonardo R. Werneck<sup>2</sup>, Ariadna Murguia-Berthier<sup>3,9</sup>, Zachariah B. Etienne<sup>2,4,5</sup>, Scott C. Noble<sup>6</sup>, and Tsvi Piran<sup>7</sup>.

Scott C. Noble<sup>6</sup>, and Tsvi Piran<sup>7</sup>.

Physics and Astronomy Department, Johns Hopkins University, Baltimore, MD 21218, USA; yzenati1@jhu.edu

Department of Physics, University of Idaho, Moscow, ID 83843, USA

Center for Interdisciplinary Exploration and Research in Astrophysics (CIERA), 1800 Sherman Ave., Evanston, IL 60201, USA

Department of Physics and Astronomy, West Virginia University, Morgantown, WV 26506, USA

Center for Gravitational Waves and Cosmology, West Virginia University, Chestnut Ridge Research Building, Morgantown, WV 26505, USA

Gravitational Astrophysics Lab, NASA Goddard Space Flight Center, Greenbelt, MD 20771, USA

Racah Institute of Physics, Hebrew University, Jerusalem 91904, Israel

Received 2023 June 15; revised 2023 August 29; accepted 2023 September 4; published 2023 November 21

#### Abstract

Many studies have found that neutron star mergers leave a fraction of the stars' mass in bound orbits surrounding the resulting massive neutron star or black hole. This mass is a site of *r*-process nucleosynthesis and can generate a wind that contributes to a kilonova. However, comparatively little is known about the dynamics determining its mass or initial structure. Here we begin to investigate these questions, starting with the origin of the disk mass. Using tracer particle as well as discretized fluid data from numerical simulations, we identify where in the neutron stars the debris came from, the paths it takes in order to escape from the neutron stars' interiors, and the times and locations at which its orbital properties diverge from those of neighboring fluid elements that end up remaining in the merged neutron star.

Unified Astronomy Thesaurus concepts: Neutron stars (1108); General relativity (641); Black holes (162); Accretion (14)

#### 1. Introduction

On 2017 August 17, the LIGO/Virgo collaboration (LVC) detected the first gravitational wave (GW) signal from a binary neutron star (BNS) merger, the GW170817 event (Abbott et al. 2017a; Villar et al. 2017). This was also the first multimessenger detection of such an event, as it was seen across the electromagnetic (EM) spectrum (Fermi, Chandra, UV, optical, IR, and radio).

From GW170817 and similar BNS mergers, we can learn about many fundamental questions in general relativity, cosmology, and astrophysics (Coulter et al. 2017; Guidorzi et al. 2017; Haggard et al. 2017; Margutti et al. 2017). For example, the distance to this event inferred from GWs was consistent with entirely independent measurements of the Hubble constant (Abbott et al. 2017b). Analysis of the GW170817 waveform led to important constraints on the nuclear equation of state (EOS; Damour et al. 2012; Bauswein et al. 2013a; Kiuchi et al. 2019; Bernuzzi 2020; Breschi et al. 2021). Its optical/IR emission gave support to the idea that such mergers could be a main channel of rapid neutron-capture (r-process) nucleosynthesis (e.g., Lattimer & Schramm 1974; Eichler et al. 1989; Metzger et al. 2010; Arcones & Thielemann 2013; Cowan et al. 2021; Pian 2023). In addition, it also demonstrated that, as predicted many years before, neutron star (NS) mergers can create short  $\gamma$ -ray bursts (see Eichler et al. 1989; Rosswog & Ramirez-Ruiz 2002; Nakar 2007; Berger 2014; Goldstein et al. 2017).

Original content from this work may be used under the terms of the Creative Commons Attribution 4.0 licence. Any further distribution of this work must maintain attribution to the author(s) and the title of the work, journal citation and DOI.

There is a strong theoretical consensus that a portion of the NSs' original mass is not held in the remnant, whether it is a massive NS (MNS) or a black hole (BH). Mass can be separated during numerous stages of a BNS merger: the late inspiral phase, the merger stage, and the subsequent evolution of the initially bound debris. Multiple mechanisms can contribute, including tidal gravity, shock heating, neutrino heating, nuclear heating, magneto-centrifugal winds (from both a debris disk and highly magnetized MNS merger remnant), and magnetohydrodynamic (MHD) turbulent dissipation (see Metzger et al. 2010; Hotokezaka et al. 2013; Fernández et al. 2015; Radice et al. 2020; Margutti & Chornock 2021; Sarin & Lasky 2021; Combi & Siegel 2023; Kiuchi et al. 2023; Most & Quataert 2023; Shibata et al. 2023).

Some of the matter that escapes from the remnant is ejected from the system altogether during the late inspiral and the merger itself. This part is called "dynamical ejecta," and it is generally ascribed to a combination of tidal forces and shock heating when the two stars come into direct contact (Hotokezaka et al. 2013). Its mass is rather small,  $\sim 10^{-3}~M_{\odot}$  (Radice et al. 2016; Fujibayashi et al. 2018; Shibata et al. 2023). Dynamical ejecta have received much attention for their possible role in producing a kilonova (KN) event, particularly those features indicating especially high outflow velocities (Metzger et al. 2010; Barnes & Kasen 2013; Radice et al. 2018a; Domoto et al. 2021; Curtis et al. 2023).

However, the same studies predict that the rest of the matter left outside the remnant is, at least temporarily, bound, and its mass is rather larger,  $\sim 0.01-0.1~M_{\odot}$ . Here we call this portion the "bound debris." It, too, likely plays a major role in NS merger phenomenology. The magnetic flux and confinement pressure needed by relativistic jets may be supplied by this debris. In addition, on rather longer timescales than dynamical ejection, the heat released inside the bound debris by nucleosynthesis and dissipation of MHD turbulence may drive a wind carrying away neutron-enriched isotopes. The

<sup>&</sup>lt;sup>8</sup> ISEF International Fellowship.

<sup>&</sup>lt;sup>9</sup> NASA Einstein fellow.

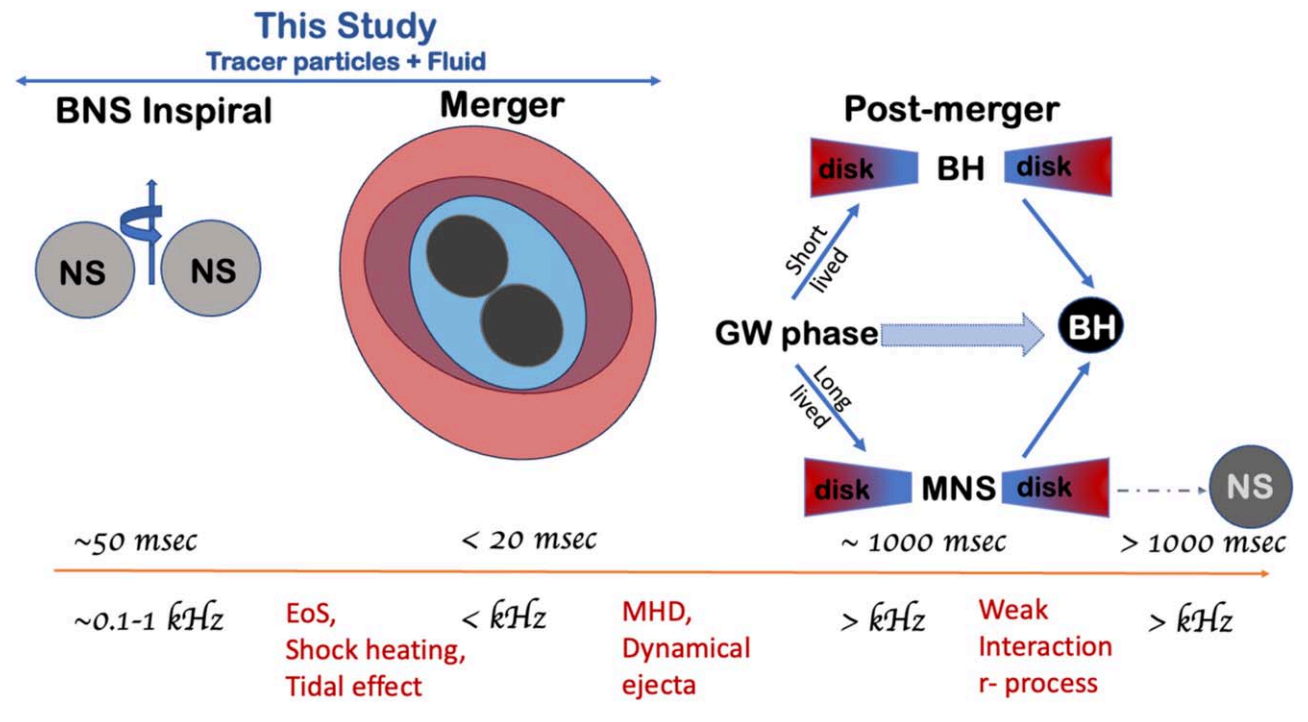


Figure 1. Schematic presentation of the different stages and outcomes of BNS mergers: from left to right, inspiral, merger, postmerger remnant plus debris disk, and, possibly, a stable NS. The timescales for each stage are shown below the corresponding sketches. The bottom line lists the GW frequency and the principal physical mechanisms of each stage.

photosphere of such a wind could also contribute to KN radiation (e.g., Rosswog & Ramirez-Ruiz 2002; Fernández et al. 2015; Just et al. 2015; Korobkin et al. 2021).

Despite its likely importance to the phenomenology of NS mergers, there has been little effort to understand the mechanisms governing how much mass is in bound orbits or the nature of its dynamical state, i.e., its distribution of angular momentum and energy. Most et al. (2021) studied the correlations between the angular momentum distribution of debris and other properties, but only for NS-BH mergers. Kiuchi et al. (2023) reported on a simulation treating an NS merger from inspiral until 1 s after the merger, but the only comment about the dynamics of disk creation they make is that the matter gains angular momentum through gravitational torques. The specific distribution of mass with angular momentum has special interest because it determines the initial surface density profile of the bound debris, which is almost certainly far from inflow equilibrium. The initial angular momentum distribution, therefore, governs the bound debris' subsequent evolution.

In this paper, we will begin the study of these issues, starting with the most basic questions: From which part(s) of the NSs is the bound debris drawn? How, and at what point in the merger, is the bound debris separated from the majority of the merged NS mass, the part that remains in the newly formed NS or is carried into the BH if one is created?

#### 2. Calculation

# 2.1. Overview

To place our calculation in context, we first review the stages of a BNS merger (see Figure 1). Once formed, an NS binary can evolve only by the emission of gravitational radiation. During very nearly the entire span of this period, the stars' separation is so large that there is no direct interaction between

them, and even gravitational tidal forces are negligible. When, however, their separation shrinks to only a few times their radii, tidal forces begin to distort them; this is the period we call the "late inspiral." Eventually, they touch, beginning the "merger proper," which creates a very MNS. Depending upon the mass and rotational state of this newly formed star, it may collapse to a BH (almost immediately or after some delay) or live for an indefinitely long time. In the course of these events, a small fraction of the initial total mass is expelled.

When the mass distribution is substantially asymmetric (the inspiral, merger, and possible collapse phases), there is no simple description of the spacetime.

Consequently, it is necessary to employ numerical relativity methods in order to follow gravitational dynamics. On the other hand, when the merged NS collapses to a BH and its structure relaxes toward Kerr, there is no need for a further solution of the Einstein field equations. For this reason, we divide our simulation of such events into two pieces. The first part is performed with the numerical relativity plus MHD code IllinoisGRMHD (Etienne et al. 2015, 2020; Werneck et al. 2023); the second part uses HARM3D+NUC (Murguia-Berthier et al. 2021). A "hand-off" procedure assures consistency between the two in terms of the spacetime and the fluid properties (Lopez Armengol et al. 2022). In the present paper, we make use of data taken only from the first part; future work in this project will employ data from the second part for studies of the bound debris' evolution, including jet launching, nucleosynthesis, and wind driving.

# 2.2. Physics Treated and Equations Solved

IllinoisGRMHD solves the equations of MHD,

$$\nabla_{\mu}(n_{\mathsf{h}}u^{\mu}) = 0, \tag{1}$$

$$\nabla_{\mu}(n_{\rm e}u^{\mu}) = \mathcal{R},\tag{2}$$

$$\nabla_{\!u} T^{\mu\nu} = \mathcal{Q} u^{\nu}, \tag{3}$$

$$\nabla_{\!\mu} {}^*\!\! F^{\mu\nu} = 0, \tag{4}$$

corresponding to the conservation of the baryon number, conservation of lepton number, conservation of energy and momentum, and the two homogeneous Maxwell equations, respectively. In coordination with the solutions of these equations, the BSSN evolution thorn Baikal solves the Einstein field equations.

In these equations,  $n_b$  ( $n_e$ ) is the baryon (lepton) number density and  $u^\mu$  is the fluid 4-velocity. The net rate of change in the lepton number  $\mathcal{R}$  is the difference between the creation rates of electron antineutrinos and neutrinos. The cooling rate  $\mathcal{Q}$  is the rate at which neutrinos (and antineutrinos) carry energy out of the gas. It is calculated from a local emission model and a leakage rate formalism (see Murguia-Berthier et al. 2021; Werneck et al. 2023, for details about the calculations of  $\mathcal{R}$  and  $\mathcal{Q}$ ).

The energy-momentum tensor is assumed to be that of a perfect fluid plus an EM contribution,

$$T^{\mu\nu} = (\rho_b h + b^2) u^{\mu} u^{\nu} + \left(P + \frac{b^2}{2}\right) g^{\mu\nu} - b^{\mu} b^{\nu}, \tag{5}$$

where  $\rho_b = m_b n_b$  is the baryon density,  $m_b$  is the mean baryon mass,  ${}^*\!F^{\mu\nu} = (1/2)\tilde{\epsilon}^{\,\mu\nu\rho\sigma}F_{\rho\sigma}$  is the dual of the Faraday tensor  $F^{\,\mu\nu}$ , and  $\tilde{\epsilon}^{\,\mu\nu\rho\sigma}$  is the Levi–Civita tensor. The parameter  $h=1+\epsilon+P/\rho_b$  is the specific enthalpy,  $\epsilon$  is the specific internal energy, and P is the fluid pressure, which is given through a tabulated form of the SFHo EOS for hot degenerate matter (O'Connor & Ott 2010).

Further,  $b^{\mu}=(4\pi)^{-1/2}B^{\mu}_{(u)}$  is the rescaled magnetic 4-vector in the fluid frame, where,

$$B_{(u)}^0 = u_i B^i / \alpha, \tag{6}$$

$$B_{(u)}^{i} = (B^{i}/\alpha + B_{(u)}^{0} u^{i})/u^{0}.$$
 (7)

Here  $B^i$  is the magnetic field in the frame normal to the hypersurface,  $b^2 \equiv b^\mu b_\mu$  is the magnetic energy density,  $g_{\mu\nu}$  is the spacetime metric, and  $\alpha$  is the lapse function. The lapse, the shift vector, and the metric are all defined on spatial hypersurfaces of constant coordinate time t. Ideal MHD  $(u_\nu F^{\mu\nu}=0)$  is assumed throughout.

In addition to solving these equations, we also follow the locations and velocities of a large number of tracer particles. By doing so, we combine the advantages of a grid-based Eulerian approach with the advantages of a moving particle Lagrangian approach (like, for example, the SPH method of Bauswein et al. 2013b). The initial positions of the tracer particles are selected by randomly choosing points p = (x, y, z) within a radius  $R_{\text{seed}} = 75$  km from the system center of mass and accepting the particle if,

$$\frac{\rho_{b}(x, y, z)}{\max \rho_{b}} > \zeta, \tag{8}$$

where  $\zeta \in [0, 1]$  is a random number. The process is repeated iteratively until all  $N_{\text{particles}} = 50,000$  have been seeded. The fact that the NSs are extremely compact and have central densities many orders of magnitude larger than that of the

surrounding gas ensures that the overwhelming majority of the tracer particles are seeded within each NS.

Once the positions  $p_n = (x_n, y_n, z_n)$  of the particles are known, where  $n = 0, 1, ..., N_{\text{particles}} - 1$ , we update them in time using,

$$\frac{dp_n^i}{dt} = v^i(p_n),\tag{9}$$

where  $v^i(p_n)$  is the fluid 3-velocity  $v^i = u^i/u^0$  interpolated to the particle's position  $p_n$ . The tracer particle positions are updated every 16 local time steps, and the 3-velocities are obtained using fourth-order Lagrange interpolation.

## 2.3. Numerical Setup

At the outer boundary, located at  $\approx$ 5670 km, we apply radiation boundary conditions to the metric quantities using Newrad (Alcubierre et al. 2003; Loffler et al. 2012) and a simple copy boundary condition for the MHD fields.

The spacetime is evolved using Baikal (Haas et al. 2022), while the MHD fields are evolved using a newly developed version of IllinoisGRMHD (Werneck et al. 2023) that supports finite-temperature, microphysical EOSs, and neutrino physics via a leakage scheme. In addition to the MHD fields, we evolve the entropy by assuming that it is conserved (see, e.g., Noble et al. 2009, for a similar strategy), an approximation that, while poor at shocks, allows us to use the entropy as a backup variable during primitive recovery (see Werneck et al. 2023, for more details).

Initial data for an equal-mass binary are constructed using LORENE (Gourgoulhon et al. 2001; Feo et al. 2017; Gourgoulhon et al. 2022), with each NS having a baryonic (gravitational) mass of 1.550  $M_{\odot}$  (1.348  $M_{\odot}$ ; see Table 1). The initial separation of the stars is 45 km and the stellar radii are  $\approx$ 9.3 km. Each is given a strong poloidal magnetic field (see, e.g., Appendix A of Etienne et al. 2015) such that  $\max{(P_{\rm mag}/P)} = \max{(b^2/2P)} = 10^{-4}$ , corresponding to  $\max{\sqrt{b^2}} = 5.05 \times 10^{15} \, G$ . The "numerical vacuum" outside the NSs is given a density  $6.25 \times 10^5 \, {\rm gm \ cm}^{-3}$ ,  $\sim 10^{-9} \times$  the NSs' central density; the total mass of this "atmosphere" that can, within the time considered here, interact with any NS material, either bound or unbound, is  $\sim 10^{-4} \times$  the binary mass. Its temperature is 0.01 MeV and its  $Y_e = 0.5$ .

Where polar coordinates are more easily interpretable, we define such a system through the simple coordinate transformation  $r^2 = (x^2 + y^2 + z^2)$ ,  $\cos \theta = z/r$ ,  $\tan \phi = y/x$ , and the x-y plane is identical to the initial binary orbital plane. In these coordinates, the polar component of the specific angular momentum is  $u_{\phi} \equiv xu_y - yu_x$ , which becomes a conserved quantity for test particles interacting only with gravity when the spacetime is axisymmetric.

The SFHO EOS table was downloaded from http://stellarcollapse.org.

<sup>11</sup> See https://github.com/zachetienne/nrpytutorial.

Table 1
Simulation Parameters for an Equal-mass, Magnetized BNS Merger Performed with IllinoisGRMHD Using a Microphysical, Finite-temperature EOS and a Neutrino Leakage Scheme

Parameter	Value
Initial data	
EOS	SFHo
NS baryonic mass	$1.550~M_{\odot}$
NS gravitational mass	$1.348~M_{\odot}$
NS radius $R_*$	9.3 km
Initial separation	45 km
$\max \sqrt{b^\mu b_\mu}$	$5.05 \times 10^{15} G$
Number of tracer particles	50,000

Postmerger	
BH dimensionless spin parameter, $\chi = a/M$	0.795
BH irreducible mass, $M_{\rm irr}$	$2.444~M_{\odot}$
BH mass, $M_{\rm BH}$	$2.726~M_{\odot}$
Mass-weighted mean $Y_{\rm e}$ ( $r=60$ km, $t\simeq17$ ms)	0.122

#### 3. Results

#### 3.1. Original Location of Matter Escaping the Merger Remnant

The most basic distinction between the tracer particles is their postmerger fate: unbound, bound, or confined within either a stable NS or a BH. We define unbound as having  $hu_t < -1$ , where h is the specific enthalpy of the fluid surrounding the particle and  $u_t$  is the particle's conserved energy. A bound particle is one with  $hu_t > -1$ , but located (in this case) outside the innermost stable circular orbit (ISCO) of the BH that forms (for this case,  $\approx 3.7 r_g = 14.8$  km from the center of the BH). We call the latter two categories "survivors."

The simplest description of the particles' postmerger position is their radial distance from the system center of mass,  $R_{i}$ ; here "postmerger" means at the end of the simulation, 17.24 ms after its start. One might expect that particles initially placed near the surface of an NS would be more likely to "survive" than particles whose starting position was deeper inside one of the stars. The relation between  $R_f$  and the distance  $R_i$  between each survivor particle and the center of its home NS is shown in Figure 2. Only  $\simeq$ 950 of the particles survive, 1.9% of the original number, representing an expelled mass  $\simeq 0.05 M_{\odot}$ . Roughly half are found outside 15  $r_e \simeq 60$  km, and  $\sim 20\%$  outside 100 km. Almost all those outside 200 km ( $\approx$ 8% of the surviving particles) are unbound, i.e., representing  $\simeq 0.004 M_{\odot}$ . Most importantly for our present purposes, there is no correlation at all between  $R_i$  and  $R_f$ except for a slight (and statistically weak) tendency for the unbound particles to originate at larger  $R_i$  than the bound particles. Note that both  $R_i$  and  $R_f$  are coordinate distances defined by  $[(x - x_c)^2 + (y - y_c)^2 + (z - z_c)^2]^{1/2}$ , where  $(x_c, y_c, z_c)$  are either the coordinates of the center of mass  $(x_c = y_c = z_c = 0)$  or the coordinates of the nearest NS center.

However, there is a sense in which particles whose initial home was at the surface of an NS are more likely to survive from the remnant. As shown by the upper panel of Figure 3, the probability that a tracer particle escapes grow for  $R_i > 8$  km, i.e., within  $\sim 1$  km of the surface. Compared to particles with smaller  $R_i$  this probability is greater by  $\sim 3-4$ . The reason why Figure 2 shows no correlation is revealed by the bottom panel of Figure 3: the probability density for the initial radius of a surviving particle is considerably larger over the range

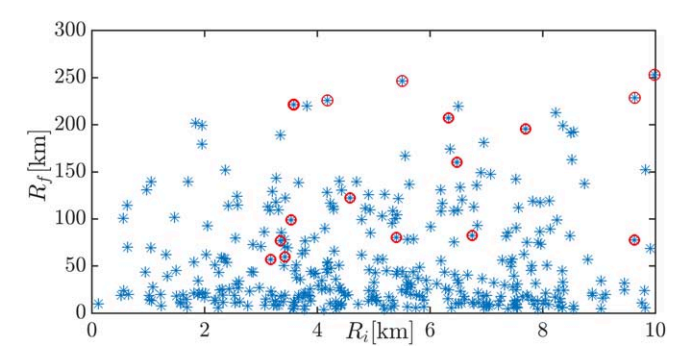


**Figure 2.** Distance  $R_j(t_f = 17.24 \text{ ms})$  from the system center of mass for the surviving tracer particles plotted against their initial distance  $R_i$  from the center of their home NS. Red circles distinguish unbound particles.

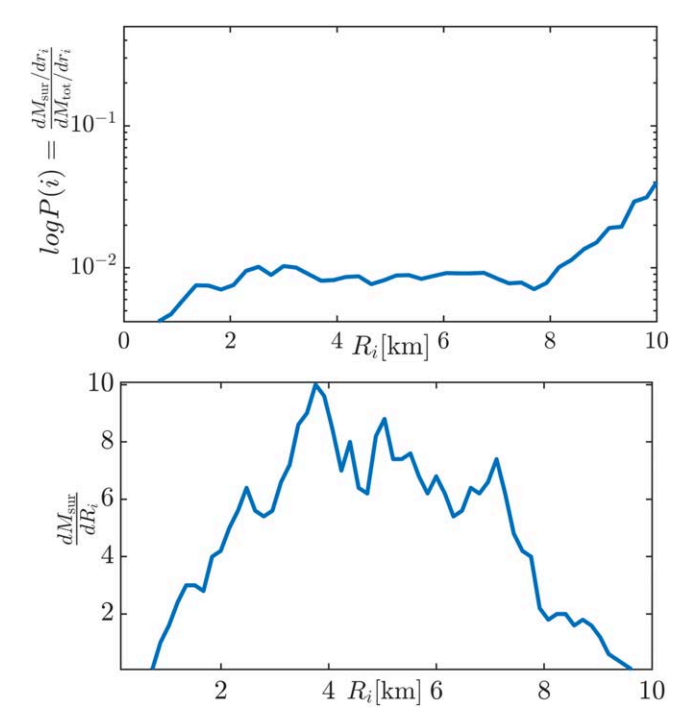


**Figure 3.** Upper panel: the probability that a particle with initial radius  $R_i$  survives BH collapse.  $M_{\rm sur}$  and  $M_{\rm tot}$  are the masses associated with the surviving and all the tracer particles, respectively. Lower panel: the probability density (in arbitrary units) that a surviving particle had initial radius  $R_i$ .

 $R_i \approx 2-8$  km than for  $R_i \gtrsim 8$  km. Even if a large fraction of all the surface particles escapes, while only a small fraction of interior particles do, there is so little mass near the surface compared to the mass in the interior that the great majority of surviving particles originate in the deep interior of an NS.

#### 3.2. Escape of Debris from the NSs' Interiors

Although answering the first question we raised, this result prompts a second: how does the bulk of the debris find its way from the deep interior of an NS to an orbit well outside the merged NS or BH? Put another way, how is it that  $\sim\!2\%$  of the matter in the interior of an NS is somehow separated from its immediate neighbors and given enough energy and angular momentum to be released from the merged NS?

In order to approach this question, we begin by identifying the time from the beginning of the simulation at which this

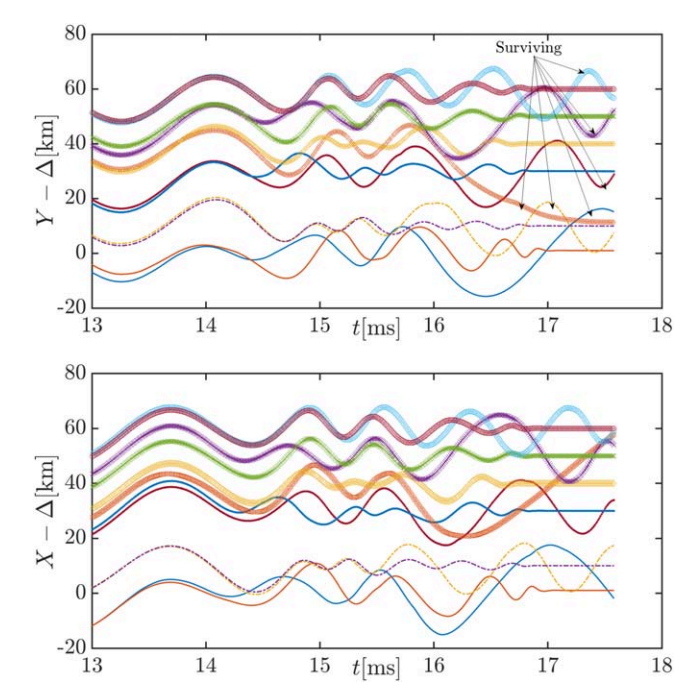


**Figure 4.** The evolution of the separation between six surviving particles and their initial close neighbors. The top panel shows how their y-coordinates evolve, the bottom panel shows the evolution of their x-coordinates. Each pair's starting location (x, y) is shifted by an arbitrary amount relative to the other pairs so that they can be visually distinguished. In some cases (e.g., the bottom two), the members of the pair start out so close together that their curves are superposed. To contrast the differing trajectories within a pair, it is best to follow the two curves beginning from t = 13 ms; designation of which survives and which does not is made by the arrows near t = 17 ms.

separation occurs. We do so by choosing a small sample of surviving particles and then pairing each with the closest nonsurviving particle in the initial state of the system. These were selected by finding survivors for which  $R_* - 2 \text{ km} < R_i < R_*$  in a single NS and were all located in different quadrants. We also constructed comparison samples varying these choices, but the results were quite similar.

In Figure 4, we display how the positions of these particles projected onto the x–y (orbital) plane evolve from t = 13.0 ms, 0.2 ms before the two stars first touch, to 17.62 ms and 1 ms after the BH forms. The oscillations reflect the rotation of the NSs, first as they orbit one another, and later as they rotate as an asymmetric merged object. As this figure shows, four of the six pairs begin to separate at  $\simeq$ 14.5 ms, while the other two do not substantially part ways until  $\simeq$ 15.5 ms. This small sample suggests the critical time for distinguishing surviving particles from captured particles is  $\simeq$ 14.5–15.5 ms; as we will see shortly, this suggestion is confirmed when we examine the data more closely.

To see what is happening during this crucial millisecond, we present images of the density and  $Y_{\rm e}$  maps at that time (Figure 5). The first of the density images (t=14.66 ms) shows the system  $\simeq 1.5$  ms after the stars first touch. Over the course of the following  $\sim 2$  ms, the configuration of the NSs changes from one in which the two stars remain partially distinguishable but are in contact over a sizable surface to one in which most of the stars' mass has taken on a much rounder shape, but a noticeable amount of gas has been expelled into spiral arms.

Complementary images of the pressure are shown in Figure 6. For these, we begin at a slightly earlier time (t = 14.50 ms) and follow it with the same three times shown in

Figure 5. Shocks can be clearly identified by surfaces on which there is a pressure discontinuity. None can be seen in the merged NS interior, but, particularly at the later times shown, polar outflows and the rotation of the asymmetric merged star can drive strong shocks in the surrounding gas (Hotokezaka et al. 2013).

Thus, the moment at which the paths of escaping and captured particles diverge is the moment when the two stars are in direct contact, but have not yet combined their masses into a single (in this case, short-lived) NS. During the first part of this stage, the mass distribution is not only highly asymmetric; it also rotates around the center of mass, so spacetime is both asymmetric and time dependent. However, during the latter part, the mass distribution becomes significantly more axisymmetric, weakening the azimuthal component of gravitational acceleration. Throughout this period, as shown by the numerous narrow regions of elevated internal energy per unit mass in Figure 6, there are many shocks, where kinetic energy is dissipated into heat, and deflection can exchange angular momentum between different fluid elements.

To understand more deeply why the surviving particles diverge from their neighboring captured particles, we now take a closer look at the six surviving particles in our sample. Figure 7 displays their x–y positions at t = 14.50 ms in relation to the fluid density in the orbital plane. Four of the six particles' locations trace a curve in the x–y plane running along the outer edge of the merged star; the other two are found along the "seam line" between the two merging stars. Their z-coordinates inform us that these particles are typically  $\sim$ (0.1–0.3)  $R_*$  out of the orbital plane, where  $R_*$  is the radius of the original NSs.

To interpret this 3D geometry, we first plot the x-y locations of all the tracer particles at this same time (blue dots in the top panel of Figure 8). The four particles in our six-member sample found along the edge of the merged star are all found in the lower hook of the "S-"curve traced out by the entire ensemble of particles; the densest parts of both hooks coincide with the plumes of gas density visible in Figure 7. The other two are in the central bar of the "S-"curve, which coincides closely with the seam line. It, therefore, appears that particles escape when they move outward through the seam region and then reach the surface. The curved portions of the "S-"curve result from the time sequence at which the particles crossed through the surface of the merged NS. Note that the orbital plane velocities of the survivor particles are primarily azimuthal, and the radial gradient in their speeds indicates that they acquire greater angular momentum as they move outward.

Further information about vertical structure can be derived from examining the locations of the particles within the bar at t=14.50 ms. Their orbital-plane coordinates all lie along the linear feature in the "S," so that their 3D positions all lie in a vertical plane defined by the line feature and the z-axis (the simple geometry of this structure is likely due to our choice of an equal-mass merger). The bottom panel of Figure 8 shows their distribution in this plane. All of the particles lie a short distance inside the outline of the merged star, a figure that is flattened in the vertical direction (see the images in the third column of Figure 5). Moreover, they are weakly concentrated toward the orbital plane and tend to avoid the polar axis.

The evolution of this structure in time is illustrated by the difference between the figures outlined by the blue and gold dots in the upper panel of Figure 8. At t = 14.50 ms, numerous particles can be found in the plane of the interstar seam, while

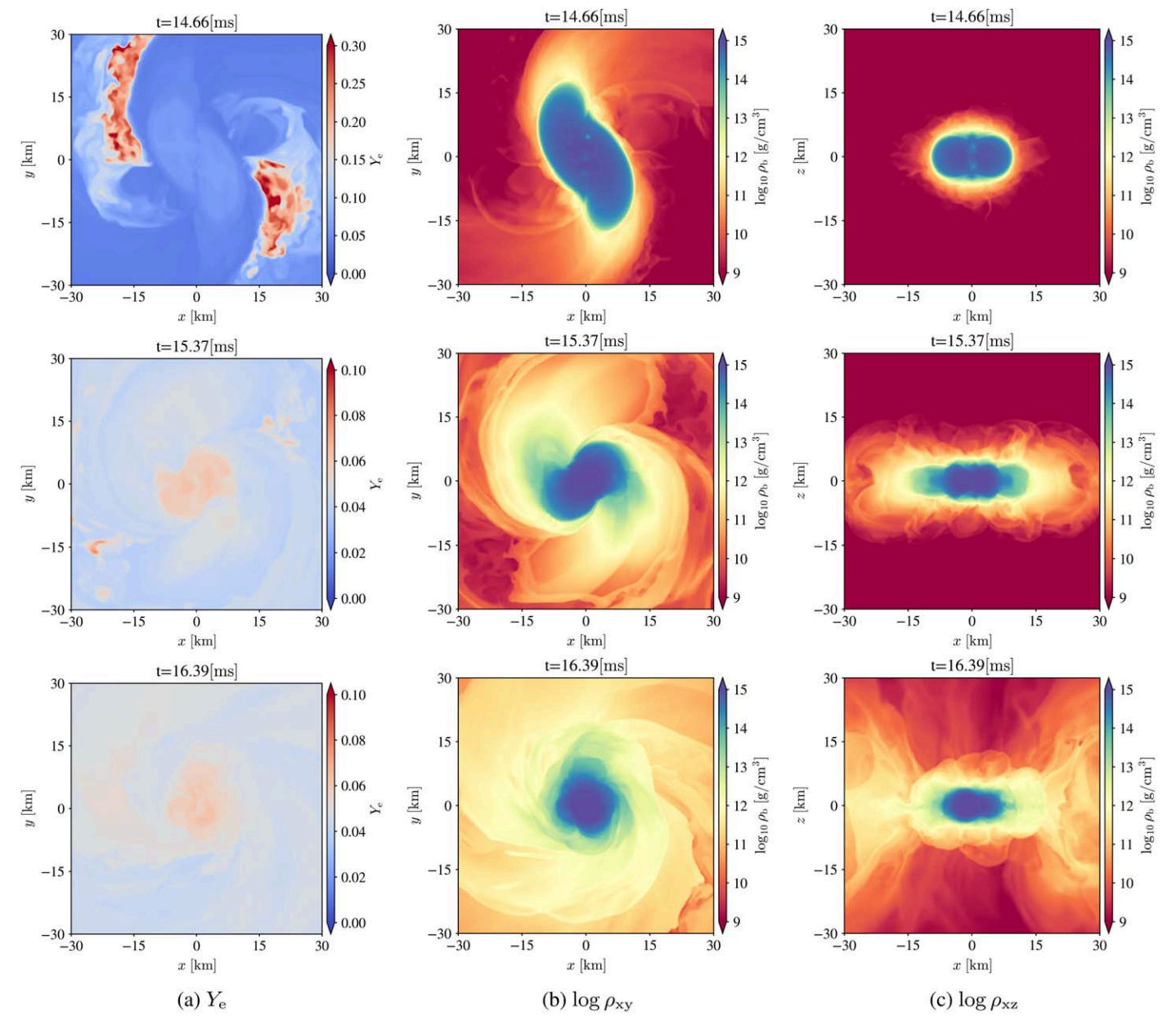


Figure 5. Evolution of the electron fraction, x–y plane mass density, and x–z plane mass density.  $Y_e$  is shown on a linear color scale (x–y plane), the mass densities on a logarithmic scale. Each quantity is presented at times 14.66 ms, 15.29 ms, and 16.31 ms; the last is shortly after the collapse to a BH. Note that the color scale for  $Y_e$  at t = 14.66 ms is different from the color scale at the other times.

the "hooks," taken together, extend over  $\sim 3\pi/2$  in azimuthal angle. Only 0.2 ms later, hardly any particles remain in the seam, while the hooks now cover all  $2\pi$  in azimuth. Thus, the period we have singled out as critical in terms of separating surviving particles from initially neighboring captured particles coincides with the time when the expulsion of matter from the seam region is completed.

The variety of paths these particles follow in order is illustrated in Figure 9, which shows three particle trajectories during the  $\sim$ 2 ms spanning the time of first contact between the stars. Just before contact, the tracer particles follow their star's orbit, but moving in and out relative to the system center of mass as the star rotates. Once the two stars come into contact (at t=13.2 ms), the character of their motion changes: now they are part of the merged NS, partaking in its rotation around the system center of mass. However, the axial fluid motions

within the contact surface permit particles to travel both outward and inward; the red path in Figure 9 is an example of the latter option. Large amplitude motions within this zone are expected because the strong shear at the boundary between the two stars excites turbulence through the Kelvin-Helmholtz instability (Rasio & Shapiro 1999; Kiuchi et al. 2014; Aguilera-Miret et al. 2022). Although our resolution is insufficient to track the shortest-wavelength modes, it can represent longer wavelengths, which lead to the eddies capable of supporting long-distance fluid transport. As can be seen in the upper panel of Figure 8, by t = 14.7 ms, only a few particles remain in the seam plane. Instead, almost all the particles destined to survive that had been inside the merger remnant at 14.5 ms are are outside it at 14.7 ms, most of them in a shell surrounding the remnant. Those that at 14.5 ms had been in the hooks of the "S" are now in either of two places: roughly half are in the shell

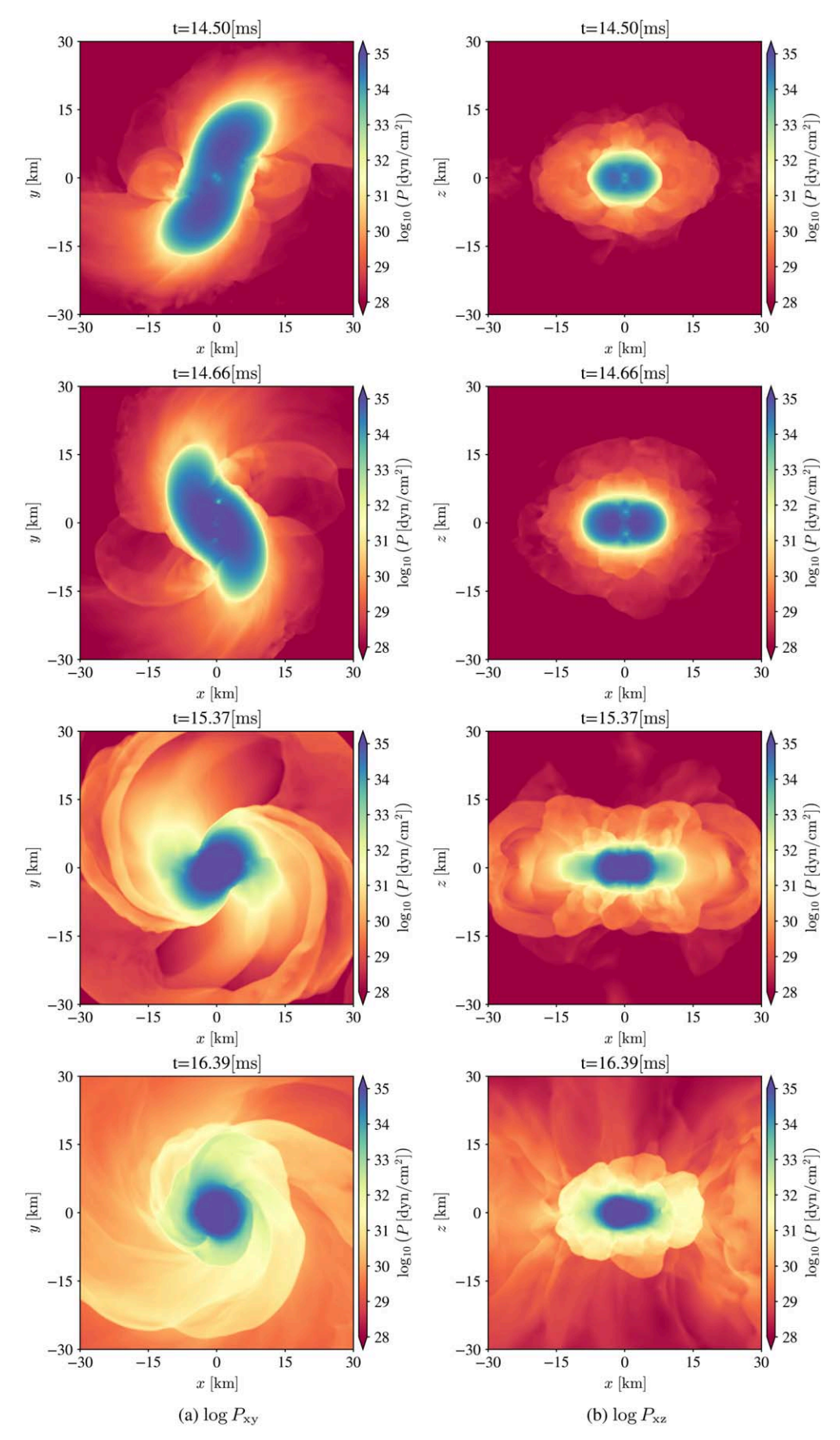
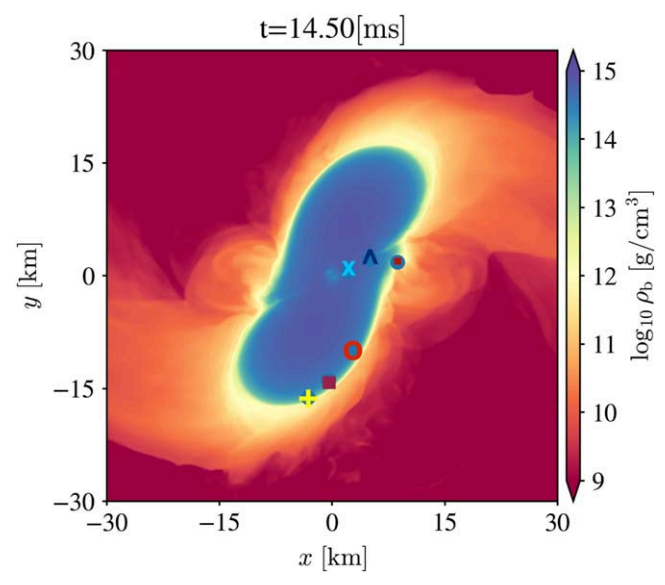


Figure 6. Evolution of the pressure P in the x-y and x-z planes, shown on a logarithmic scale at times 14.50 ms, 14.66 ms, 15.37 ms, and 16.39 ms.



**Figure 7.** The x-y locations of the same six surviving particles shown in Figure 4 superposed on the t = 14.50 ms density map. Their z-coordinates are z = 2.558, -2.225, -3.097, 2.182, 1.738, and 3.504 km for the particles shown as a plus sign, a square, a circle, a dot, an "X," and a caret, respectively.

surrounding the remnant, many of them having moved inward to do so; the other half are outside the boundary of the figure.

# 3.3. Separation of Surviving Particles from Neighboring Particles

The surviving particles are  $\simeq 2\%$  of the NSs' mass; as can be seen in Figure 8,  $\simeq 90\%$  have reached positions just outside the star by  $\sim 1$  ms after contact. From the data illustrated in Figure 4, it is clear that the captured particles that began close to the survivors are still close to them at this time. It immediately follows that the distinction between survivors and the captured matter is accomplished in two stages. First, a few percent of the total mass of NSs is conveyed to locations outside the stars by motion through the contact surface. Second, when this matter reaches locations immediately outside the merged star, local effects divide this mass into two subsets: one that escapes, the other remaining with the merged star.

How this distinction is made is portrayed in Figure 10. For the first  $\sim$ 2 ms shown, the angular momenta of the surviving particles are very similar to those of their matching captured particles; both oscillate as a result of the NSs' rotation. At around 14–15 ms, the angular momentum of surviving particles begins to rise (as shown by the arrows in Figure 8), while the angular momentum of the neighboring particles that remain with the star for the long run in general do not change appreciably, and for the few exceptions, any increase in angular momentum is lost a short time later. This growth in survivor particle angular momentum finishes shortly before collapse to a BH (t = 16.6 ms). By then, the surviving particles' angular momentum is  $\sim$ 2–10 $\times$  the angular momentum of the captured particles that started out from locations very near them.

That these results are characteristic of all the surviving particles are shown in Figure 11. A small number of particles have large excursions in  $u_{\phi}$  during the inspiral, but the overwhelming majority of particles follow the pattern of the small sample we have chosen for particular study.

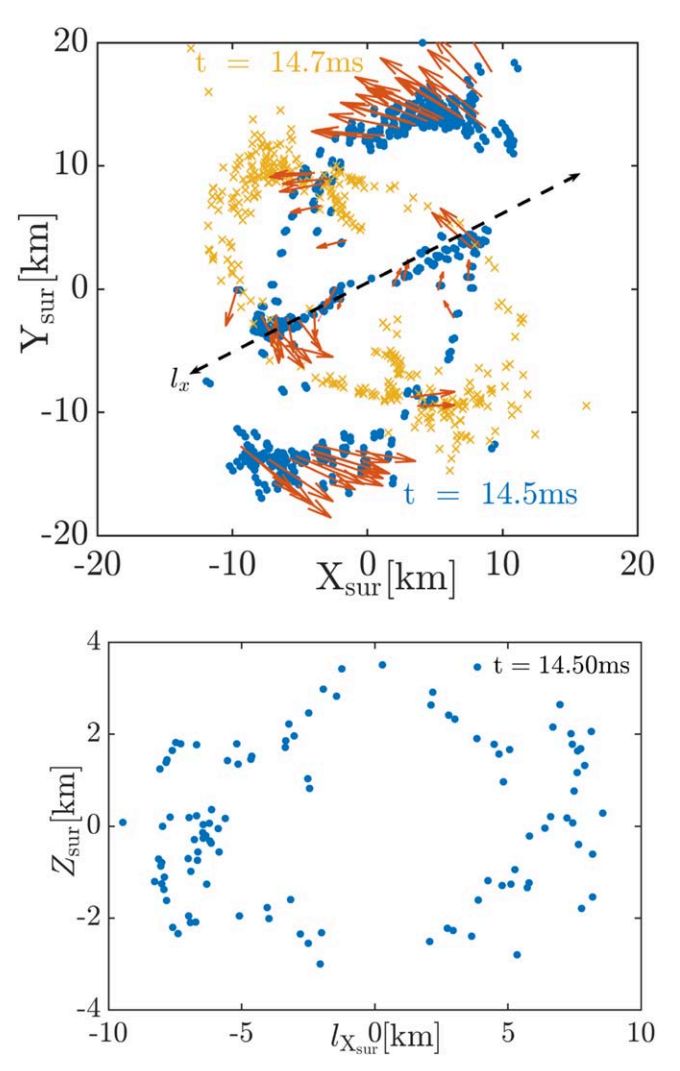


**Figure 8.** Top: position in the x–y plane of the surviving particles at t = 14.506 ms (blue dots) and at t = 14.705 ms (yellow crosses). The line labeled " $l_x$ " is fit to the line-like feature in the middle of the "**S**-"shape at t = 14.50 ms. The red arrows illustrate the x–y velocities of a random sample of surviving particles at t = 14.50 ms; the arrows' lengths are proportional to the speeds of the particles' orbital plane motion. Bottom: positions in the  $l_x$ –z plane of the surviving particles in the line-like feature at t = 14.50 ms.

The torques creating the change in angular momentum could be the result of nonaxisymmetric gravity (Hotokezaka et al. 2013; Radice et al. 2018b; Fujibayashi et al. 2018; Shibata et al. 2023), smooth pressure gradients, or shocks (Hotokezaka et al. 2011, 2013; Sekiguchi et al. 2016). If the magnetic field is as strong as Kiuchi et al. (2014) found (but not seen here), magnetic forces might also contribute. Shocks can be recognized by the sharp steps in angular momentum evident in Figure 10 as well as the cusps seen in the trajectories of Figure 9, which might be associated with shock features visible in the later images of Figure 6. Both gravitational acceleration and smooth pressure gradients could lead to smooth portions of trajectories. The short timescale smaller fluctuations in  $u_{\phi}$ shown in Figure 10 are more likely associated with pressure gradients than with gravity because there are many short length-scale density gradients, whereas the gravitational field is the result of the global stress-energy distribution. The general upward trend could be associated with nonaxisymmetric gravity, and its end at  $t \approx 16$  ms roughly coincides with the axisymmetrizing of the merged NS (see Figure 5). On the other

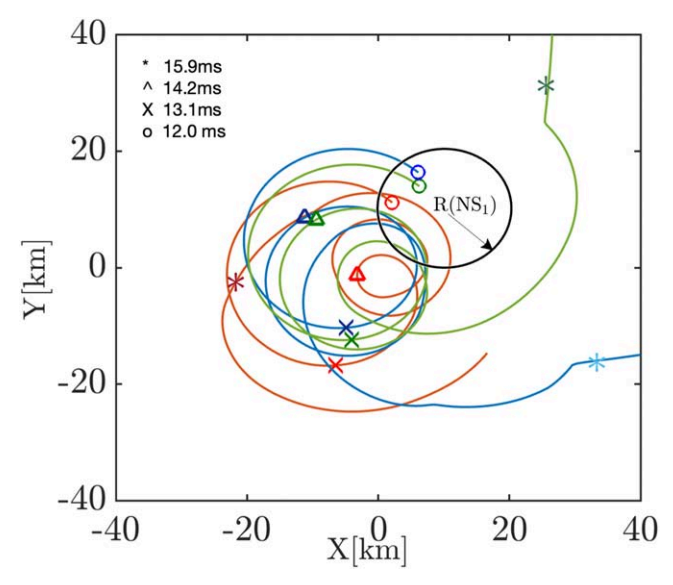


**Figure 9.** Motion in (x, y) of three surviving particles (blue, green, and red dotted paths) from t = 12 ms to t = 16.6 ms, when the star collapses to a BH. The black circle shows the outline of their parent star at t = 12 ms. Cusps are the signature of shock deflection.

hand, it is unclear how a gravitational effect would distinguish the particles that ultimately survive from the nearby particles that are ultimately captured; nonaxisymmetric gravity could become important only after other dynamics place fluid elements in the regions where gravitational torques exist. In this context, it is also worth noting that the captured particles show much less short timescale fluctuation in  $u_{\phi}$ , suggesting that the regions through which they travel have much smoother density and pressure distributions. This would, of course, be a natural consequence of staying closer to the merged star.

#### 4. Discussion

# 4.1. Initial Electron Fraction in the Bound Debris

The electron fraction  $Y_{\rm e}$ , the ratio of the number of protons  $n_p$  to the total number of nucleons, is one of the key quantities for determining the elements synthesized over longer timescales in the bound debris. Through this influence, it is also the key to determining the opacity of the optical/UV photosphere where the KN emission is radiated (see Barnes & Kasen 2013; Hotokezaka et al. 2013; Siegel & Metzger 2017; Radice et al. 2018a).

If there were special locations in the NSs that contributed disproportionately to the bound debris, the distribution of mass with electron fraction  $dM/dY_e$  in its initial state could be quite different from  $dM/dY_e$  in the NSs as a whole. However, we have shown that, in rough terms, the probability that a fluid element inside one of the NSs is expelled from the remnant is very nearly constant for all radii between ≈1 and ≈8 km, a region containing the great majority of mass in the star. There are only two exceptions to this constant probability. One is a spherical shell  $\simeq 1$  km thick at the outside of the star, where the probability of escape rises to a few times greater than elsewhere. The other is a sphere of radius  $\sim$ 1 km at the center of the star, where the escape probability is  $\lesssim 0.1 \times$  the value in the star's bulk. Consequently, the shape of the dM/d  $Y_e$ distribution of the entire mass of each premerger NS should be a good starting point for following the  $dM/dY_e$  distribution in each star's contribution to the bound debris.

On the other hand, it should also be borne in mind that  $Y_e$  can be affected by events happening during the merger and while the bound debris travel from the merged NS to its place in the surrounding disk. Shock heating in the merger and during the subsequent evolution of the merger remnant can raise the matter temperature above 10 MeV. In such a high-temperature environment, electron–positron pair creation can substantially raise the rate of the reaction  $e^+ + n \rightarrow p^+ + \bar{\nu}_e$ , thereby increasing  $Y_e$ . Neutrino irradiation, within the merged star, as the gas travels to the disk, and in the disk can also raise  $Y_e$  via reactions like  $\nu_e + n \rightarrow p^+ + e^-$ . The degree to which any of these mechanisms may or may not alter  $Y_e$  requires further investigation (Shibata et al. 2023).

#### 4.2. Parameter Dependence

Quantitative details in the single calculation on which we base our results could change for different values of the principal system parameters, the mass ratio q and the total mass M. In particular, the bilateral symmetry so evident in the images of Figures 5, 7, and 8 will be broken when  $q \neq 1$ . It has also long been known (Oechslin & Janka 2006; Shibata et al. 2023) that the total mass removed from the merger remnant generally increases for smaller values of q, but there can be exceptions (Fujibayashi et al. 2023). Thus, the total amount of bound debris mass in this simulation may be on the lower end of what might be expected for a merger of this total mass.

The results should also depend on M. If it is so large that the merger results in immediate collapse to a BH, the amount of expelled mass, both in dynamical ejecta and bound debris, would be much smaller. Moreover, because the tidal gravity contribution to the expelled mass would be a larger fraction of the total, the bound fraction would likely be considerably smaller. On the other hand, if M were small enough for the merged NS to survive for a longer time, the expelled mass could be rather larger.

The combination of different M and different q can alter the results quantitatively in several ways. Smaller values of both imply particularly small mass for the less-massive star, giving it both a lower mean density and a less centrally concentrated internal density profile (see Lattimer & Prakash 2007; Bauswein et al. 2012; Shibata et al. 2021; Raithel et al. 2022). Relatively large tidal mass loss would likely follow. Larger M and smaller q could enhance the contribution of the contact shock if the larger mass star has  $\gtrsim 2~M_{\odot}$  because for such large masses, the radius of the NS diminishes, whereas it hardly changes (for most EOSs) for masses between  $\sim$ 0.7 and  $\sim$ 2  $M_{\odot}$  (Kashyap et al. 2022). The sense in which these changes tip the balance between bound and unbound debris requires a detailed calculation to determine.

## 4.3. Uncertainty in the EOS

Although the gravitational waveform measured in the event GW170817 has helped prune the long list of proposed nuclear EOSs (see Hotokezaka et al. 2011; Bauswein et al. 2013a; Radice et al. 2018b), there still remain many candidates. Our quantitative results could be altered in several ways if a different EOS applies. First, the internal density profile of an equilibrium NS is sensitive to the EOS, and that could alter the probability of escape as a function of radius. Second, when the two stars come into contact, the pressure of the shocked region between the two depends on the EOS. Stiffer EOSs support

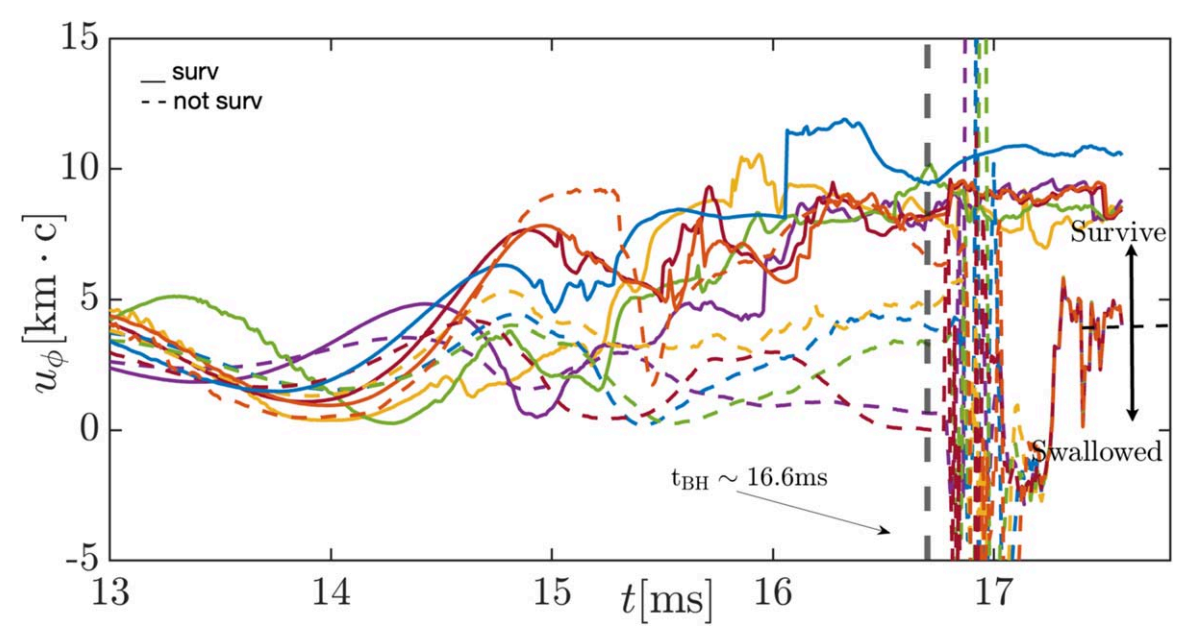
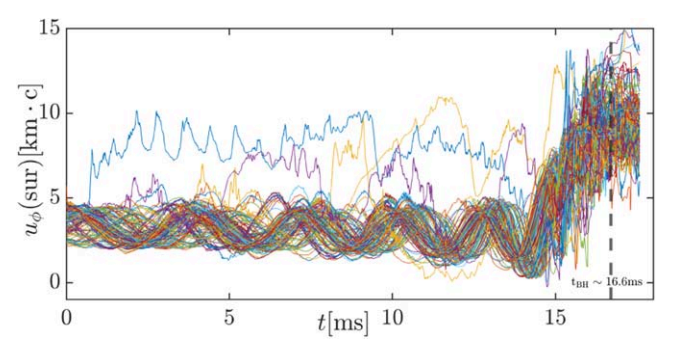


Figure 10. Time dependence of the angular momentum  $u_{\phi}$  for our sample of six pairs of particles. Survivors are shown with solid lines, and captured particles with dashed lines; matching colors identify the pairs. The time of collapse to a BH, 16.6 ms is marked with a gray dashed vertical line; for captured particles after that time, the physical significance of  $u_{\phi}$  is unclear.



**Figure 11.** Evolution of  $u_{\phi}$ , the conserved angular momentum component in an axisymmetric spacetime, for a large sample of the survivor tracer particles: 220 particles selected at random. The small number of surviving particles with higher  $u_{\phi}$  and noisy  $u_{\phi}$  histories during the premerger inspiral (blue, yellow, and purple lines) were initially located very close to the surface of one or the other of the NSs.

larger NSs that strike each other with lower velocity, diminishing the postshock temperature (Hotokezaka et al. 2011); on the other hand, a larger ratio between pressure and internal energy density would make the shocked region wider and enlarge the pressure contrast between the shocked region and the surface of the merged star. Third, the EOS governs both the critical mass dividing quick collapse from a longer-lived merger NS and the time to collapse if rapid collapse is, indeed, the result (Bauswein et al. 2013a; Radice et al. 2018b; Margalit et al. 2022). A longer lifetime for the merged NS likely leads to more escaping mass, and the ratio of bound to unbound mass could change over this span of time. Thus, different EOSs could lead to changes in both the total mass removed from the remnant and how it is divided into bound and unbound portions.

#### 4.4. Potential Complications Due to Resolution

Spatial resolution has the potential to affect our results in several ways. Radice et al. (2018a) showed that refining the

finest grid scale from 185 to 123 m decreased the bound debris mass by a factor of 3.5 when the SFHo EOS was used, but led to almost no change in the velocity distribution of the unbound ejecta. Whether the angular momentum and energy distributions for the bound debris are equally independent of resolution is unclear. This result may (or may not) be related to the fact that Kelvin–Helmholtz modes are linearly unstable for wavenumbers  $k \lesssim 1/d$ , where d is the thickness of the shear region (Chandrasekhar 1961). If the shear region is narrower than a simulation's resolution can describe, the smallest-scale linearly unstable eddies are absent.

The same question regarding resolution of the Kelvin–Helmholtz instability also has implications for the rate of growth of the magnetic field (Kiuchi et al. 2015). Although these are important for the longer-term evolution of NS mergers, they are less so for the situation considered here. Partly this is because we began with a comparatively strong field,  $\sim\!10^{15}$  G. More importantly, however, even if the field were as strong as that achieved in Kiuchi et al. (2015), its pressure inside the star would still be only  $\sim\!10^{-4}\times$  the gas pressure (see Figure 6), and therefore unlikely to be of much dynamical importance.

#### 5. Conclusions

In much of the literature on NS mergers, when matter that escapes being confined within the merger remnant is discussed, the focus is solely on the unbound fraction. This fraction is then further divided into two categories, "dynamical" and "secular" (sometimes called "postmerger;" Metzger et al. 2010; Fernández et al. 2015; Siegel & Metzger 2017; Radice et al. 2018a; Fujibayashi et al. 2018). "Dynamical" refers to the material expelled during the merger itself, whether by tidal forces, shocks heating gas, or neutrinos that heat or push the gas. "Secular" refers to matter driven off the disk of bound debris many milliseconds after the merger.

However, the majority of the matter outside the merger remnant remains bound to the system, forming the disk that is the source of the secular ejecta and may also support any jet that forms. Hitherto, the mechanisms by which this material leaves the merging NSs and is deposited in the debris disk have gone largely unexamined. Here we have determined the origin of the bound debris within the NSs and examined how its fate is distinguished from that of matter remaining inside the merged star.

In particular, by making use of the complementary information provided by Eulerian fluid data and Lagrangian tracer particle data, we have uncovered several surprising facts about the process by which matter is expelled from merging NSs.

- 1. The probability that a given parcel of mass leaves the merger remnant is almost, but not quite, independent of its location inside the premerger NSs. Matter placed near the surface of an NS is considerably more likely than most matter to be expelled, but there is so much more matter in the bulk of the star that, despite its lower escape probability, nearly all the escaping matter, whether bound or unbound, has its origin deep in a star's interior.
- 2. Turbulent motions within the "seam" surface formed when the two stars touch can mix matter from a wide range of initial depths within the stars. These same motions transport some of this matter through the seam plane to the surface of the merged star.
- 3. A significant amount of matter is brought out to the surface of the merged NS but does not escape. Which matter is captured and which escapes depends on details of the shock structure in the region where the matter that has been squeezed outward by the shock between the two merging stars reaches the surface.
- 4. The surviving matter acquires significant additional angular momentum as it leaves the remnant. It is likely that torques due to the nonaxisymmetric gravity of the merged NS, smooth pressure gradients, and shocks all contribute.
- 5. All of these processes occur within a few milliseconds after the stars first touch.

Thus, we have shown that the process by which matter escapes the remnant created by an NS merger is considerably more complex and subtle than previously envisioned. Because the disk of bound matter circulating around the merged NS or BH is far from inflow equilibrium, its subsequent evolution depends on what sort of nonequilibrium structure it is given. Understanding the mechanisms regulating this structure is, therefore, an essential part of understanding many of the dramatic observational properties of NS mergers—jets, KNe, and *r*-process nucleosynthesis.

#### Acknowledgments

This work was partially supported by NASA TCAN grant NNH17ZDA001N. We thank the anonymous referee for a number of comments that improved the paper. In addition, Y.Z. thanks Prof. Will Farr, Prof. Yuri Levin, and Mor Rozner for their helpful discussions. L.R.W. and Z.B.E. gratefully acknowledge support from NSF awards PHY-1806596, PHY-2110352, and OAC-2004311, as well as NASA award ISFM-80NSSC18K0538. A.M.-B. is supported by NASA through the NASA Hubble Fellowship grant HST-HF2-51487.001-A

awarded by the Space Telescope Science Institute, which is operated by the Association of Universities for Research in Astronomy, Inc., for NASA, under contract NAS5-26555. T.P. was supported in part by ERC advanced grant "Multijets." This research made use of Idaho National Laboratory computing resources which are supported by the Office of Nuclear Energy of the U.S. Department of Energy and the Nuclear Science User Facilities under Contract No. DE-AC07-05ID14517.

Software: astropy (Astropy Collaboration et al. 2018), IllinoisGRMHD (Etienne et al. 2015), Numpy (Harris et al. 2020), and Matplotlib (Hunter 2007).

#### ORCID iDs

Yossef Zenati https://orcid.org/0000-0002-0632-8897
Julian H. Krolik https://orcid.org/0000-0002-2995-7717
Leonardo R. Werneck https://orcid.org/0000-0002-4541-8553
Ariadna Murguia-Berthier https://orcid.org/0000-0003-2333-6116
Zachariah B. Etienne https://orcid.org/0000-0002-6838-9185

Scott C. Noble https://orcid.org/0000-0003-3547-8306 Tsvi Piran https://orcid.org/0000-0002-7964-5420

References Abbott, B. P., Abbott, R., Abbott, T. D., et al. 2017a, Natur, 551, 85 Abbott, B. P., Abbott, R., Abbott, T. D., et al. 2017b, ApJL, 848, L12 Aguilera-Miret, R., Viganò, D., & Palenzuela, C. 2022, ApJL, 926, L31 Alcubierre, M., Bruegmann, B., Diener, P., et al. 2003, PhRvD, 67, 084023 Arcones, A., & Thielemann, F. K. 2013, JPhG, 40, 013201 Astropy Collaboration, Price-Whelan, A. M., Sipőcz, B. M., et al. 2018, AJ, 156, 123 Barnes, J., & Kasen, D. 2013, ApJ, 775, 18 Bauswein, A., Baumgarte, T. W., & Janka, H. T. 2013a, PhRvL, 111, 131101 Bauswein, A., Goriely, S., & Janka, H. T. 2013b, ApJ, 773, 78 Bauswein, A., Janka, H. T., Hebeler, K., & Schwenk, A. 2012, PhRvD, 86, 063001 Berger, E. 2014, ARA&A, 52, 43 Bernuzzi, S. 2020, GReGr, 52, 108 Breschi, M., Perego, A., Bernuzzi, S., et al. 2021, MNRAS, 505, 1661 Chandrasekhar, S. 1961, Hydrodynamic and Hydromagnetic Stability (Oxford: Clarendon) Combi, L., & Siegel, D. M. 2023, arXiv:2303.12284 Coulter, D. A., Foley, R. J., Kilpatrick, C. D., et al. 2017, Sci, 358, 1556 Cowan, J. J., Sneden, C., Lawler, J. E., et al. 2021, RvMP, 93, 015002 Curtis, S., Mösta, P., Wu, Z., et al. 2023, MNRAS, 518, 5313 Damour, T., Nagar, A., & Villain, L. 2012, PhRvD, 85, 123007 Domoto, N., Tanaka, M., Wanajo, S., & Kawaguchi, K. 2021, ApJ, 913, 26 Eichler, D., Livio, M., Piran, T., & Schramm, D. N. 1989, Natur, 340, 126 Etienne, Z. B., Paschalidis, V., Haas, R., Moesta, P., & Shapiro, S. L. 2020, IllinoisGRMHD: GRMHD code for dynamical spacetimes, Astrophysics Source Code Library, ascl:2004.003 Etienne, Z. B., Paschalidis, V., Haas, R., Mösta, P., & Shapiro, S. L. 2015, COGra, 32, 175009 Feo, A., De Pietri, R., Maione, F., & Löffler, F. 2017, CQGra, 34, 034001 Fernández, R., Kasen, D., Metzger, B. D., & Quataert, E. 2015, MNRAS, 446, 750 Fujibayashi, S., Kiuchi, K., Nishimura, N., Sekiguchi, Y., & Shibata, M. 2018, ApJ, 860, 64 Fujibayashi, S., Kiuchi, K., Wanajo, S., et al. 2023, ApJ, 942, 39 Goldstein, A., Veres, P., Burns, E., et al. 2017, ApJL, 848, L14 Gourgoulhon, E., Grandclément, P., & Novak, J., 2022 LORENE: Langage Objet pour la RElativité NumériquE, https://lorene.obspm.fr/ Gourgoulhon, E., Grandclement, P., Taniguchi, K., Marck, J.-A., & Bonazzola, S. 2001, PhRvD, 63, 064029 Guidorzi, C., Margutti, R., Brout, D., et al. 2017, ApJL, 851, L36 Haas, R., Cheng, C.-H., Diener, P., et al. 2022, The Einstein Toolkit, The

"Sophie Kowalevski" release, ET\_2022\_11, Zenodo, doi:10.5281/zenodo.

7245853

```
Haggard, D., Nynka, M., Ruan, J. J., et al. 2017, ApJL, 848, L25
Harris, C. R., Millman, K. J., van der Walt, S. J., et al. 2020, Natur, 585, 357
Hotokezaka, K., Kiuchi, K., Kyutoku, K., et al. 2013, PhRvD, 87, 024001
Hotokezaka, K., Kyutoku, K., Okawa, H., Shibata, M., & Kiuchi, K. 2011,
  PhRvD, 83, 124008
Hunter, J. D. 2007, CSE, 9, 90
Just, O., Bauswein, A., Ardevol Pulpillo, R., Goriely, S., & Janka, H. T. 2015,
    MNRAS, 448, 541
Kashyap, R., Das, A., Radice, D., et al. 2022, PhRvD, 105, 103022
Kiuchi, K., Cerdá-Durán, P., Kyutoku, K., Sekiguchi, Y., & Shibata, M. 2015,
   PhRvD, 92, 124034
Kiuchi, K., Fujibayashi, S., Hayashi, K., et al. 2023, PhRvL, 131, 011401
Kiuchi, K., Kyutoku, K., Sekiguchi, Y., Shibata, M., & Wada, T. 2014,
   PhRvD, 90, 041502
Kiuchi, K., Kyutoku, K., Shibata, M., & Taniguchi, K. 2019, ApJL, 876, L31
Korobkin, O., Wollaeger, R., Fryer, C., et al. 2021, ApJ, 910, 116
Lattimer, J. M., & Prakash, M. 2007, PhR, 442, 109
Lattimer, J. M., & Schramm, D. N. 1974, ApJL, 192, L145
Loffler, F., Faber, J., Bentivegna, E., et al. 2012, CQGra, 29, 115001
Lopez Armengol, F. G., Etienne, Z. B., Noble, S. C., et al. 2022, PhRvD, 106,
  083015
Margalit, B., Jermyn, A. S., Metzger, B. D., Roberts, L. F., & Quataert, E.
   2022, ApJ, 939, 51
Margutti, R., Berger, E., Fong, W., et al. 2017, ApJL, 848, L20
Margutti, R., & Chornock, R. 2021, ARA&A, 59, 155
Metzger, B. D., Martínez-Pinedo, G., Darbha, S., et al. 2010, MNRAS,
```

406, 2650

```
Most, E. R., Papenfort, L. J., Tootle, S. D., & Rezzolla, L. 2021, MNRAS,
  506, 3511
Most, E. R., & Quataert, E. 2023, ApJL, 947, L15
Murguia-Berthier, A., Noble, S. C., Roberts, L. F., et al. 2021, ApJ, 919, 95
Nakar, E. 2007, PhR, 442, 166
Noble, S. C., Krolik, J. H., & Hawley, J. F. 2009, ApJ, 692, 411
O'Connor, E., & Ott, C. D. 2010, CQGra, 27, 114103
Oechslin, R., & Janka, H. T. 2006, MNRAS, 368, 1489
Pian, E. 2023, Univ, 9, 105
Radice, D., Bernuzzi, S., & Perego, A. 2020, ARNPS, 70, 95
Radice, D., Galeazzi, F., Lippuner, J., et al. 2016, MNRAS, 460, 3255
Radice, D., Perego, A., Hotokezaka, K., et al. 2018a, ApJ, 869, 130
Radice, D., Perego, A., Zappa, F., & Bernuzzi, S. 2018b, ApJL, 852, L29
Raithel, C. A., Espino, P., & Paschalidis, V. 2022, MNRAS, 516, 4792
Rasio, F. A., & Shapiro, S. L. 1999, CQGra, 16, R1
Rosswog, S., & Ramirez-Ruiz, E. 2002, MNRAS, 336, L7
Sarin, N., & Lasky, P. D. 2021, GReGr, 53, 59
Schnetter, E., Hawley, S. H., & Hawke, I. 2004, CQGra, 21, 1465
Sekiguchi, Y., Kiuchi, K., Kyutoku, K., Shibata, M., & Taniguchi, K. 2016,
   PhRvD, 93, 124046
Shibata, M., Fujibayashi, S., Hayashi, K., Kiuchi, K., & Wanajo, S. 2023,
  IAUS, 362, 190
Shibata, M., Fujibayashi, S., & Sekiguchi, Y. 2021, PhRvD, 104, 063026
Siegel, D. M., & Metzger, B. D. 2017, PhRvL, 119, 231102
Villar, V. A., Guillochon, J., Berger, E., et al. 2017, ApJL, 851, L21
Werneck, L. R., Etienne, Z. B., Murguia-Berthier, A., et al. 2023, PhRvD, 107,
```